4
$Ni_{1-x}Zn_xFe_2O_4$ Spinel Ferrite Materials and their Composites for 2-12.4GHz MW Absorption

4.1 INTRODUCTION

Spinel ferrites ($MeFe_2O_4$), with cubical closed packed crystal structure exhibit the close crystallographic resemblance with natural occurring spinel $MgAl_2O_4$ [Bragg, 1915] and is the reason for their identification afterwards. The unit cell of $MeFe_2O_4$ crystal lattice consists of 32 sites of O^{2-}anions at Face Centered Cubic (FCC) positions. There are two types of interstitial sites: (i) Tetrahedral sites (A); where 04 nearest O^{2-} anions are coordinated (ii) Octahedral sites (B); where 06 nearest O^{2-} anions are coordinated as shown in Figure 4.1. In a unit cell total 64 tetrahedral and 32 octahedral sites are present. Out of these, only 8 tetrahedral and 16 octahedral sites are occupied, and make the system electrically neutral [Goldman, 1990]. Each spinel ferrite unit cell is made of 08 formula units ($MeFe_2O_4$; where Me= Fe^{2+}, Mg^{2+}, Ni^{2+}, Co^{2+}, $Zn^{2+}$and their combinations), with total contribution of 08 Me^{2+} cations, 16 Fe^{3+} cations and 32 O^{2-} anions. All the Me^{2+} cations are located at available 08 tetragonal sites and Fe^{3+} cations are situated at total available 16 octahedral sites in form of $(Me)^{tet}[Fe_2]^{oct}O_4$. A structure with such atomic configuration is termed as normal spinel arrangement e.g. $ZnFe_2O_4$. However, if the Fe^{3+} cation occupies both 08 tetragonal and octahedral sites and Me^{2+}cation settles at octahedral sites $(Fe)^{tet}[Me, Fe]^{oct}O_4$, such arrangement is called inverse spinel configuration e.g. $NiFe_2O_4$.

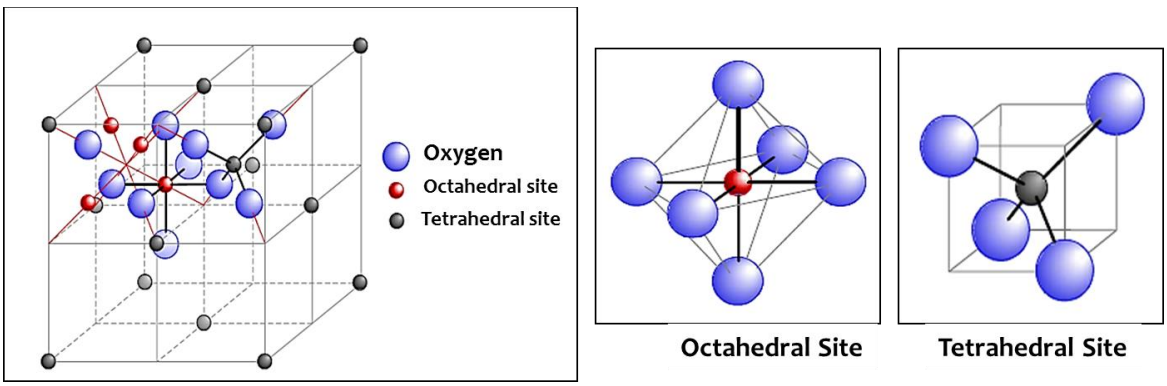

Figure 4.1 : Crystal structure of spinel ferrite system

$NiFe_2O_4$ represents the inverse spinel crystal structure $(Fe^{3+})^{tet}[Ni^{2+}, Fe^{3+}]^{oct}O_4$ with antiparallel spin arrangements of cations' at tetragonal (A) and orthogonal (B) sites. The magnetic properties in such system arises due to the complex exchange interaction between different cations (Ni^{2+}, Fe^{3+}), situated at A and B sites. In such inverse spinel crystal structure, the oxygen ion is situated in between the different cations, resulting into increased Ni^{2+}-O-Fe^{3+}inter-cationic distance. This oxygen leads to the exchange coupling between Ni^{2+} and Fe^{3+} cations, known as super exchange interaction, which depends on cationic distance Ni^{2+}-O, O-Fe^{3+} and bending angle of Ni^{2+}-O-Fe^{3+} arrangement. The exchange energy between A and B cationic sites is given by Eq. (4.1)

$$E_{ex} = -2JS_AS_B\cos\Phi \qquad (4.1)$$

Where, J is exchange integral, S_A and S_B are resultant spin vectors of A and B cationic sites and Φ is bending angle between spin vectors. Thus, the bending angle of π will lead to the maximum super-exchange between the cations and thus enhanced magnetic interaction. The exchange interaction of A and B cations via O^{2-} anion in spinel structure is depicted in Figure 4.2 schematically, with interionic bond length and bending angles, respectively. A-O-A and B-O-B bending angles are 90° and 79°38′ respectively, which are relatively small for strong interaction, resulting into weak antiferromagnetic nature for such cation configurations. Whereas, A-O-B exchange interaction is the strongest among different exchange interactions in these systems because of large bending angle ~154°34′, close to the angle π, desired for maximum super-exchange interaction.

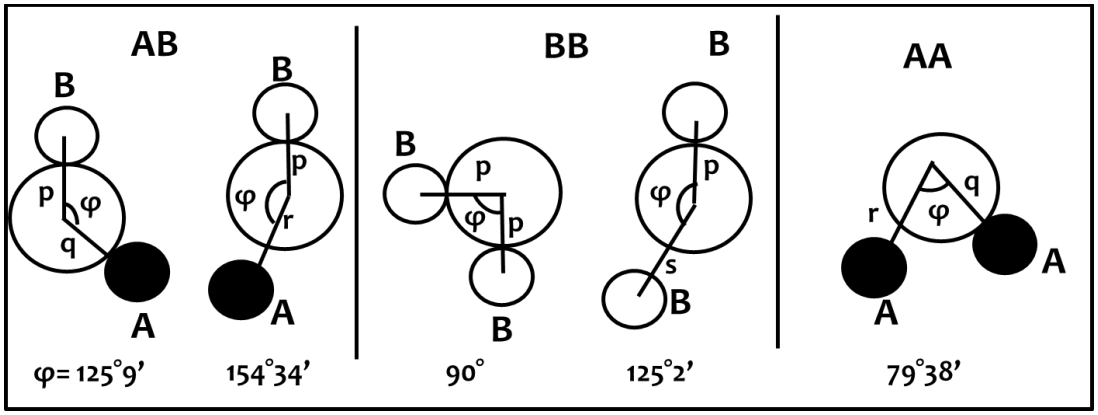

Figure 4.2: Depiction of interionic bond length and bending angle in different configuration of spinel structures (Source: Smit and Wijn, 1959)

The ferromagnetic spins at A and B are aligned in antiparallel direction with net non-zero magnetization resulting into ferrimagnetic nature of such inverse spinel structures. The net magnetization (M_T) in Ni ferrite system is the result of the difference of magnetization at octahedral (M_B) and tetrahedral sites (M_A), giving rise to the ferrimagnetism. The spin arrangement in Ni-Zn system, and thus effective saturation magnetization, can be altered by substituting Zn^{2+} ions at the tetragonal Fe^{3+}sites $(Zn_x^{2+}Fe_{1-x}^{3+})^{tet}[Ni_{1-x}^{2+}, Fe_{1+x}^{3+}]^{oct}O_4$. Due to the co-existence of Ni^{2+} and Zn^{2+}, this system is termed as mixed spinel ferrite. The Zn substitution affects the magnetic properties significantly [Fawzi *et al.*, 2010; Moulson and Herbert, 1990]. While in the case of $ZnFe_2O_4$ ferrite, where non-magnetic Zn^{2+} ions fully occupy the A site, the system converts in antiferromagnetic magnetic ordering, due to the absence of unpaired spins at A site and the antiparallel spin arrangement at B sites results into zero net magnetization. The probable changes in magnetic properties are summarized in Table 4.1 as a function of different cation distribution in Ni-Zn ferrite system. The onset of MW absorption mechnism in magnetic materials has already been discussed in chapter 2, explaining the physical paramters and their contribution into the MW absorption. The inverse spincel $Ni_{1-x}Zn_xFe_2O_4$ ferrite system may provide better opportunities for their applications in RCS reduction of military objects in the desired frequency range of MW spectrum, because of their tunable electrical [Dzunuzovic *et al.*, 2015; Razzitte *et al.*, 2004], magnetic [Krishna *et al.*, 2012; Costa *et al.*, 2003] and microwave absorption properties [Amiri *et al.*, 2011; Huang *et al.*, 2015; Kakirde *et al.*, 2008; Kim *et al.*, 1994]. This Ni-Zn inverse spinel ferrite system offers excellent MW absorption properties in 2-8 GHz at much less absorber thickness as compared to other dielectric/magnetic materials. The possible Zn^{2+} ion variation in $Ni_{1-x}Zn_xFe_2O_4$ provides a better control on the magnetic properties, essential for MW absorption application. The following sections discuss the work carried out for the optimized synthesis of $Ni_{1-x}Zn_xFe_2O_4$ process and their physical properties in view of MW absorption applications. Further, the optimized $Ni_{1-x}Zn_xFe_2O_4$ (x = 0.50) sample has been used to investigate the impact of loading fraction in rubber composites to realize the MW absorber product for possible applications.

Table 4.1: Variation in magnetic moment with distribution of cations in Ni-Zn ferrite system

S. No.		Tetrahedral site (A)		Octahedral site (B)		
	Concentration of Zn^{2+} ion in $Ni_{1-x}Zn_xFe_2O_4$ (x)	**Position of ions**	**Magnetic moment**	**Position of ions**	**Direction of Magnetic moment**	**Net Magnetic Moment**
1.	x=1 ($ZnFe_2O_4$)	Zn^{2+}	--	Fe^{2+}	↑ ↓	⊗
2.	x= 0 ($NiFe_2O_4$)	Fe^{2+}	↓	Fe^{3+}, Ni^{2+}	↑ ↑	↑
3	x=0.5 ($Ni_{0.5}Zn_{0.5}Fe_2O_4$)	Fe^{3+}, Zn^{2+}	↓	Fe^{3+}, Ni^{2+}	↑ ↑	↑

4.2 EXPERIMENTAL PROCEDURE

The $Ni_{1-x}Zn_xFe_2O_4$ ferrite powder samples were prepared using gel to carbonate precipitation method. The co-precipitations of divalent cations (Ni^{2+}, Zn^{2+}) as fine particles of carbonates within the hydrated gels of ferric hydroxide is carried out by adding the alkali solution into the mixed metal salt ions in gel to carbonate precipitation process. For the synthesis of 50g batch of $Ni_{1-x}Zn_xFe_2O_4$, 1M solution of Iron (III) Chloride anhydrate ($FeCl_3$) (Merck CAS No. 7705-08-0), Nickel (II) Chloride ($NiCl_2.6H_2O$) (Merck CAS No. 7718-54-9), and Zinc Chloride ($ZnCl_2$) (Merck CAS No. 7646-85-7) were mixed stoichiometrically in 01 liter distilled water, for each composition of ferrite powder as mentioned in Table 4.2.

Table 4.2: Stoichiometric ratio of salt precursors for preparation of ferrite powders (50g batch size)

S. No.	Ferrite Composition of $Ni_{1-x}Zn_xFe_2O_4$	$FeCl_3$	$NiCl_2.6H_2O$	$ZnCl_2$
1.	x=0, $NiFe_2O_4$	69.21g	50.71g	NIL
2.	x=0.25, $Ni_{0.75}Zn_{0.25}Fe_2O_4$	68.70g	37.76g	7.21g
3.	x=0.50, $Ni_{0.5}Zn_{0.5}Fe_2O_4$	68.24g	25g	14.33g
4.	x=0.75, $Ni_{0.25}Zn_{0.75}Fe_2O_4$	67.75g	12.41g	21.35g

The aqueous solution of salt precursors was heated at ~120°C for 20 minutes. The precipitation of this solution was accomplished by adding drop wise 1M Sodium Carbonate (Na_2CO_3) solution (Merck CAS No. 497-19-8). The solution was continuously stirred during precipitation process. The pH of the final solution was maintained at ~9 to realize the co-precipitation. The precipitate was filtered and washed with hot distilled water several times (14 – 15 times) to wash out any entrapped chloride ions. Thus collected precipitate was dried in an oven at ~120°C for 2h in the air ambient conditions. The dried powder consists of crystalline Ni/Zn carbonates in ferric oxide amorphous medium. Initially, the composite powder was air annealed at 650°C for 3h at the heating rate of ~10°C/minute and cooled down to room temperature with natural cooling rate. The obtained powder was ground and sieved through 100 mesh size (~149 μm). In the second step, annealing of 650°C dried powder was carried out in air at 950°C at the heating rate of ~8°C/minute for 3h. Further, the collected powder was ground to get fine powder. In the final annealing stage 950°C annealed powder was further annealed at ~1250°C for 3h with heating rate of ~5°C/minutes. The annealed powder was obtained as the lumped agglomerates, due to the high temperature annealing, which resulted into fusion of ferrite granules. To get the fine powder, crushing and milling of the lumped powder was carried

out using mixer grinder and analytical mill. Sieving of powder was done through 100 µm size sieve. A series of $Ni_{1-x}Zn_xFe_2O_4$ spinel ferrites with x= 0, 0.25, 0.50 and 0.75 was prepared using the similar processing steps, to understand the effect of composition on physical properties and the impact on MW absorption properties as a function of Zn atomic fraction in $Ni_{1-x}Zn_xFe_2O_4$.

X-ray diffraction (XRD) studies were carried out to ascertain the spinel crystal phase, annealing temperature dependence on crystal phase and the phase purity of all $Ni_{1-x}Zn_xFe_2O_4$ ferrite samples, annealed at 650°C/950°C/1250°C. The XRD spectra were recorded in the range of 20-80° using Cu K_α X-ray incident radiation with wavelength λ = 1.5406 A°. FTIR studies were carried out on these samples to ensure the chemical purity of materials. The room temperature field versus magnetization (M-H) studies was carried out to evaluate the temperature and composition dependent magnetic properties, for all the prepared samples in the magnetic field range of -2KOe to 2KOe using Vibrating Sample Magnetometers (VSM). Complex relative permittivity and permeability values were measured using two port Vector Network Analyzer in MW frequency range of 2-12.4 GHz. For the frequency 2-6 GHz coaxial transmission line technique was used whereas for J band (6-8.2 GHz) and X band (8.2-12.4 GHz), waveguide transmission line technique was used to evaluate the material's parameters. Based on these EM parameters, magnetic loss tangent ($\tan\delta_m$) values were calculated for all the ferrite samples. Optimized composition of ferrite having optimal MW absorption properties (in the present case $Ni_{0.5}Zn_{0.5}Fe_2O_4$) was selected for fabrication of rubber based composites.

As discussed in chapter 3, the ferrite loaded NBR composites were prepared by using rubber processing facilities viz. Two Roll Mixing Mill (TRMM) and High Temperature Compression and Moulding Press (HTCMP). In the present study, ferrite powder was dispersed in rubber matrix at different 50, 60, 70 and 80wt% loading fractions. Beyond 80 wt% ferrite loading, fabrication of rubber composite was not possible due to brittleness of final composite samples. Table 4.3 summarizes the compositions of different ferrite loaded rubber composites with respective sample identification. The volume content of ferrite powder in the composite samples increases drastically with increase in loading e.g. 80 wt% ferrite loaded sample FMAR80 have four fold ferrite content as compared to 50 wt% loaded sample FMAR50.

Table 4.3: List of $Ni_{0.5}Zn_{0.5}Fe_2O_4$ ferrite loaded rubber composites

S. No.	Sample Code	Quantity of NBR (g)	Wt% of $Ni_{0.5}Zn_{0.5}Fe_2O_4$ ferrite in compound	Quantity of ferrite powder (g)	Enhancement in filler loading as compared to sample FMAR50 (x)
1	FMAR50	30	50	30	1.00
2	FMAR60	30	60	45	1.50
3	FMAR70	30	70	70	2.33
4	FMAR80	30	80	120	4.00

EM parameters of rubber composites were computed using waveguide transmission line technique over S (2-4 GHz), G (4-6 GHz), J (6-8 GHz) and X (8-12 GHz) frequency bands. Based on the measured parameters, reflection loss (R.L.) values were calculated for all the ferrite loaded composites at different thicknesses and optimized the matched thickness for maximum R.L. values.

4.3 RESULTS AND DISCUSSIONS

4.3.1 X-ray Diffraction Analysis

The X-ray diffraction spectra are shown in Figures 4.3(a)-(d) for all $Ni_{1-x}Zn_xFe_2O_4$ (x=0, 0.25, 0.50, 0.75) ferrite powder samples, annealed at 650°C, 950°C and 1250°C temperatures, respectively. The presence of characteristic peaks indexed by (220), (311), (222), (400), (422), (511)

and (440) planes confirm the spinel phase for all the ferrite compositions annealed at 650°C. Further, the observed broadening in XRD spectral peaks for powder annealed at 650°C indicates the formation of fine particles for all the ferrite compositions. Furthermore, the XRD peak intensity increases with increase in annealing temperature to 950°C and 1250°C, while the respective diffraction peaks broadening has reduced, suggesting the grain growth of ferrite particles for all the compositions.

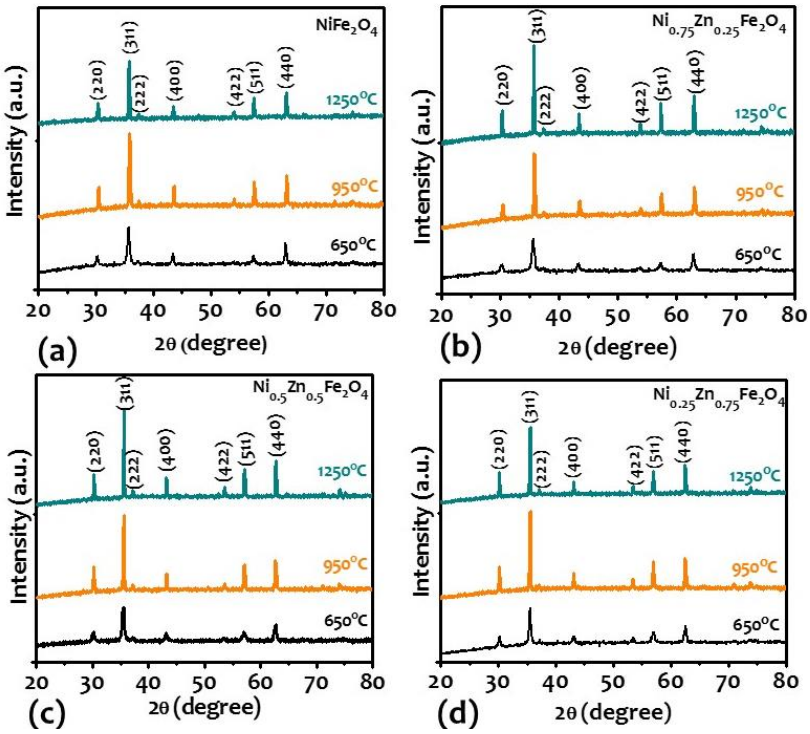

Figure 4.3 : XRD pattern of ferrite compositions annealed at different elevated temperatures of 650°C, 950°C and 1250°C (a) $NiFe_2O_4$ (b) $Ni_{0.75}Zn_{0.25}Fe_2O_4$ (c) $Ni_{0.5}Zn_{0.5}Fe_2O_4$ (d) $Ni_{0.75}Zn_{0.25}Fe_2O_4$

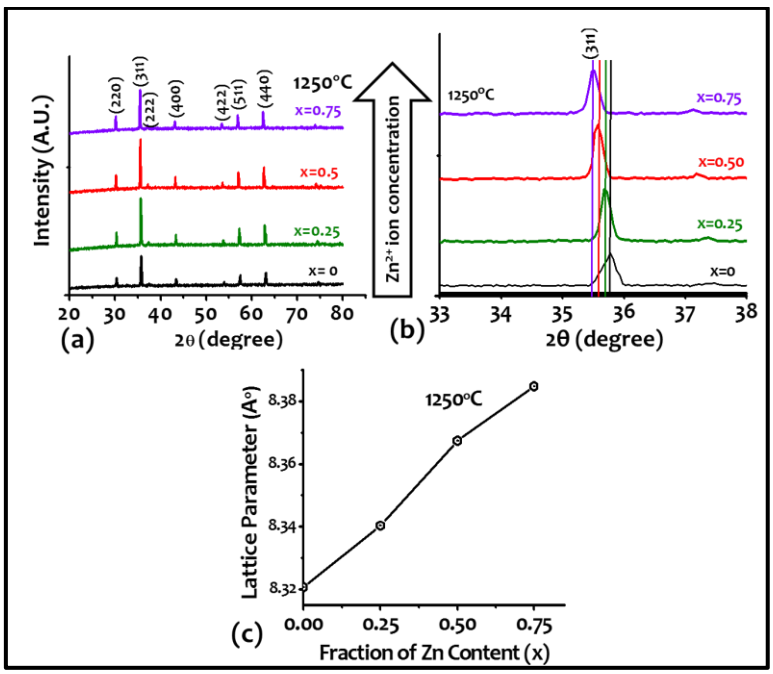

Figure 4.4 : (a) XRD pattern of different ferrite compositions annealed at 1250°C (b) Shift of XRD peak corresponding to (331) plane with Zn^{2+} ion concentration (c) Change in lattice parameters with fraction of Zn^{2+} ion content

Figure 4.4(a) shows XRD spectra for $Ni_{1-x}Zn_xFe_2O_4$ ferrite compositions, annealed at 1250°C, with different Zn^{2+} ion concentration (x= 0, 0.25, 0.5 and 0.75). These XRD graphs shown in Figure 4.4(a) confirm the formation of phase pure spinel crystallographic structure without any residual phase/composition for all the Zn^{2+} substituted $Ni_{1-x}Zn_xFe_2O_4$ compositions in the present study. It has been observed that the diffraction peaks are shifted towards lower angle with an increase in Zn^{2+} ion concentration. A representative peak shift corresponding to (311) plane is shown in Figure 4.4(b). A shift of 0.26° in 2θ has been observed from $NiFe_2O_4$ to $Ni_{0.25}Zn_{0.75}Fe_2O_4$. The observed shifting of the diffraction peaks in the present study towards lower angle is attributed to the enlargement of lattice parameter (a) of the cubic crystal structure for these inverse spinel compounds, as summarized in Figure 4.4(c). We found that the lattice parameter varies from 8.321A° for pure Ni ferrite (x=0) to 8.385A° for $Ni_{0.25}Zn_{0.75}Fe_2O_4$ ferrite (x=0.75) composition. The increased lattice parameter (a) with Zn^{2+} ion concentration is attributed to the replacement of Ni^{2+} ion (0.78A°) with the large sized Zn^{2+} ion (0.83A°), resulting into the lattice strain in the cubic spinel ferrite structure [Zhang *et al.*, 2013; Nandapure *et al.*, 2012; Jalaly *et al.*, 2010]

4.3.2 FTIR Analysis

A representative FTIR pattern is shown in Figure 4.5(a) for $Ni_{1-x}Zn_xFe_2O_4$ (x=0.5) ferrite powders annealed at 650°C, 950°C and 1250°C temperatures. The spectra consists of two characteristic vibrational absorption peaks at ~586 cm^{-1} and ~425 cm^{-1} due to Me-O (Me= Fe/Ni/Zn) stretching vibrational bonds at tetragonal and orthogonal sites of spinel structure, respectively, in all the annealed samples and results are consistent with the reported literature [Singh *et al.*, 2012; Leng *et al.*, 2013]. There are no other absorption peaks observed in spectra for these samples, indicating that the prepared ferrite powders are phase pure. FTIR spectra for Zn^{2+} ion substituted ferrite samples are shown in Figure 4.5. These measurements suggest that the absorption peaks are shifting towards lower wavenumber with increasing Zn dopant concentration. For example, the absorption peak corresponding to the tetragonal spinel phase has shifted from 620 cm^{-1} to 558 cm^{-1} for $Ni_{1-x}Zn_xFe_2O_4$ ferrite system from x= 0 to 0.75. The vibrational frequency (in wave number) depends on reduced mass (μ) of associated chemical bond ($\bar{\upsilon}\ \alpha\ 1/\sqrt{\mu}$). This observed shifting in FTIR peak is attributed to enhancement of reduced mass of Me-O stretching vibrational bond due to replacement of heavier Zn^{2+} ion (65.38 g/mol) in place of Ni^{2+} ion (58.693 g/mol) with increment of x.

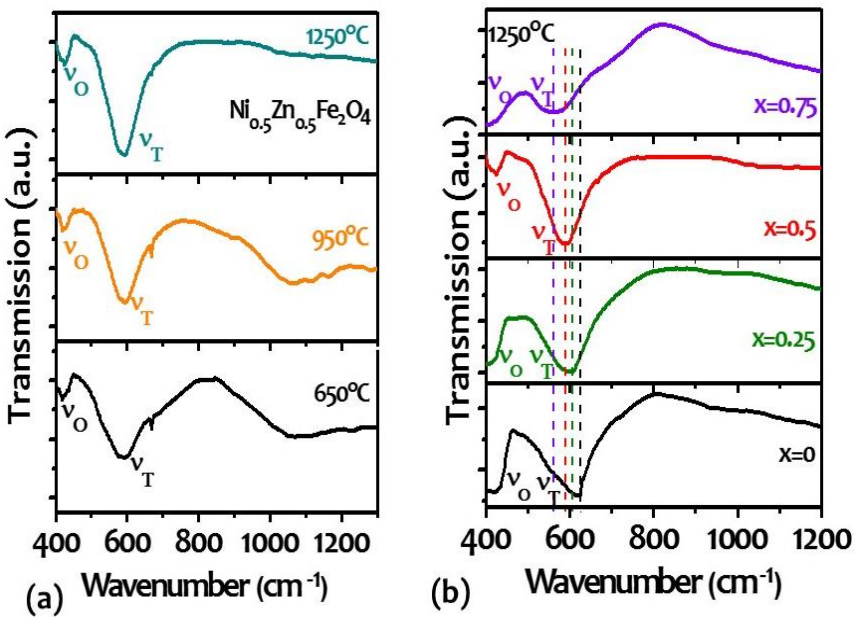

Figure 4.5 : (a) FTIR pattern of $Ni_{0.5}Zn_{0.5}Fe_2O_4$ ferrite powders annealed at elevated temperatures of 650 °C, 950°C and 1250°C (b) Variation in FTIR spectra for $Ni_{1-x}Zn_xFe_2O_4$ ferrite powder with Zn^{2+} ion concentration (x=0, 0.25, 0.5 and 0.75)

4.3.3 Morphological Analysis

SEM micrographs are shown in Figures 4.6(a)-(b) for $Ni_{1-x}Zn_xFe_2O_4$ (x= 0 and 0.5) annealed at 650°C, 950°C and 1250°C samples respectively. The 650°C annealed ferrite powders show fine microstructure with spherical particle morphology. This particle morphology has increased with annealing temperature as can be seen in 950°C annealed sample micrograph, Fig. 4.6a(ii) and b(ii). Further, there is a significant grain growth of ferrite powders with distorted spherical morphology for the powder samples annealed at 1250°C. The average crystalline size was found ~1.4µm for ferrite powder sample annealed at 1250°C. However, $Ni_{1-x}Zn_xFe_2O_4$(x=0.50) shows larger grain size with fused particles, as shown in Figure 4.6b(iii). This observation indicates that the addition of Zn promotes the grain growth in ferrite composition and observations are consistent with reported literature [Smith, 1959].

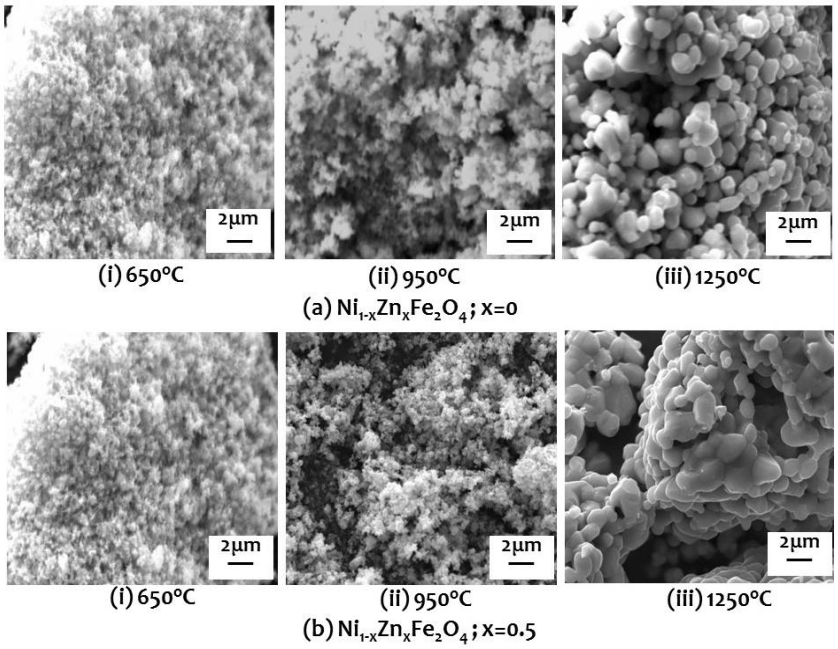

Figure 4.6 : SEM micrograph of $Ni_{1-x}Zn_xFe_2O_4$ powder annealed at elevated temperatures of 650°C, 950°C and 1250°C for (a) x=0 (b) x=0.5

4.3.4 Elemental Analysis

The elemental compositions were recorded using energy dispersive X-ray analysis (EDX) system for $Ni_{1-x}Zn_xFe_2O_4$ (x=0 and x=0.5) samples, annealed at 1250°C and results are shown in Figures 4.7(a)-(b). The elemental EDX peaks were observed for Ni, Fe and O in both undoped and Zn doped ferrite samples, whereas additional peaks corresponding to Zn were observed for Zn doped $Ni_{0.5}Zn_{0.5}Fe_2O_4$ sample, as shown in Figure 4.7(b). The detailed atomic elemental fraction is summarized in Table 4.4 for both these samples. These results suggest that the synthesized ferrite material is stoichiometric without any compositional non-uniformity.

Table 4.4: Elemental analysis of $NiFe_2O_4$ and $Ni_{0.5}Zn_{0.5}Fe_2O_4$ ferrite compositions

S. No.	Ferrite composition	Atomic %			
		Ni	Zn	Fe	O
1.	$NiFe_2O_4$	14.24%	--	37.34%	48.42%
2.	$Ni_{0.5}Zn_{0.5}Fe_2O_4$	6.65%	6.34%	31.45%	55.55%

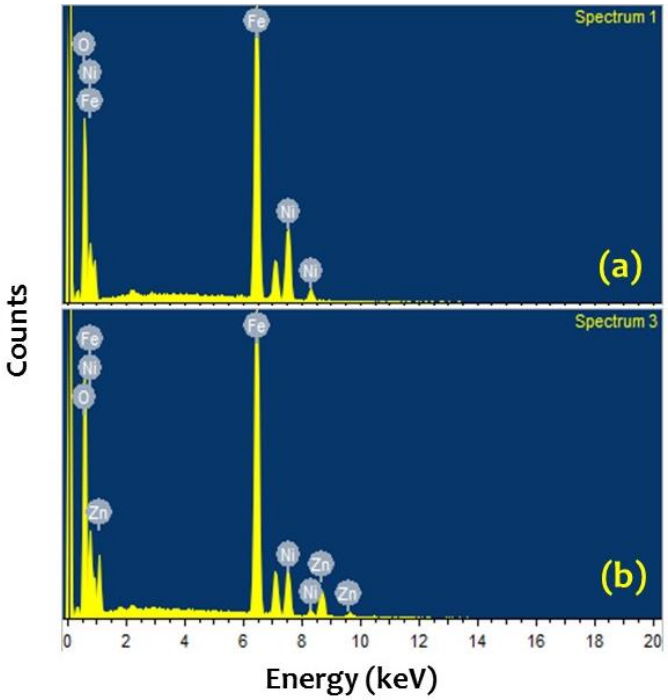

Figure 4.7 : EDS spectra of $Ni_{1-x}Zn_xFe_2O_4$ powder annealed at elevated temperatures of 1250°C for (a) x=0 (b) x=0.5

4.3.5 Magnetic Studies

The room temperature field dependent magnetic measurements are summarized in Figure 4.8 for $Ni_{1-x}Zn_xFe_2O_4$ (x=0, 0.25, 0.50 and 0.75) ferrite powders annealed at 650°C, 950°C and 1250°C temperatures. All these compositions show ferrimagnetic behavior with different saturation magnetization (M_s) and coercive field (H_c) values. The variation of M_s and H_c are plotted in Figure 4.9(a)-(b) as a function of annealing temperature and Zn^{2+} ion concentration. The saturation magnetization increases with increasing the annealing temperature for all these compositions except for the $Ni_{0.25}Zn_{0.75}Fe_2O_4$ ferrite powder. Marginal decrease in saturation magnetization has been observed for this composition (x=0.75) while annealed at 950°C and then a small increase in value for annealing at a higher temperature ~ 1250°C. Simultaneously, the coercive field values decrease with increase in annealing temperature for all the compositions except for ferrite powder with high Zn content (x=0.75). This behavior can be understood with the ordered distribution of ions in tetrahedral and octahedral sites in the inverse spinel crystallographic phase, which enhances with increasing annealing temperature.

The cation ordering has increased with increasing temperature, as observed in XRD measurements Figure 4.3, which resulted into the higher saturation magnetization with higher annealing temperatures. The saturation magnetic values are the largest for all compositions, annealed at 1250°C, due to the appropriate cation distribution in the preferred lattice sites with cubic crystal structure [Peelamedu *et al.*, 2003]. Further, saturation magnetization has also increased initially with Zn^{2+} ion concentration and a significant decrease has been observed beyond x=0.5 for ferrite compositions, as shown in Figure 4.9(b). At low concentration of Zn^{2+} ions, the spin occupancy has reduced at A (tetrahedral) sites due to the non-magnetic Zn^{2+} ions, however, net magnetization has increased due to the shift of Fe^{3+} ions from A site to B (octahedral) sites. On further increase in Zn^{2+} substitution beyond x=0.5, the effective spin contribution is less at A site due to the non-availability of spin sites. This reduces the super-exchange interaction between A-B cation sites, leading to decrease in magnetization value, as observed in the present study [Zhang *et al.*, 2013; Krishna *et al.*, 2012]. Moreover, the annealing temperature has favored grain growth, resulting in the enhanced number of domain walls/ or even larger domains within the grains. The contribution of a domain wall in magnetization/demagnetization process dominates against domain rotation, as domain wall movement is less energetic than the domain

wall rotation. Therefore, such energy competition between domain rotation and domain wall movement in larger grains has led to the low coercive field values for compositions annealed at higher temperature i.e. 1250°C. Further, the observed reduction in coercive field values is attributed to the decrease in magneto-crystalline anisotropy with Zn substitution [Verma *et al.*, 2000].

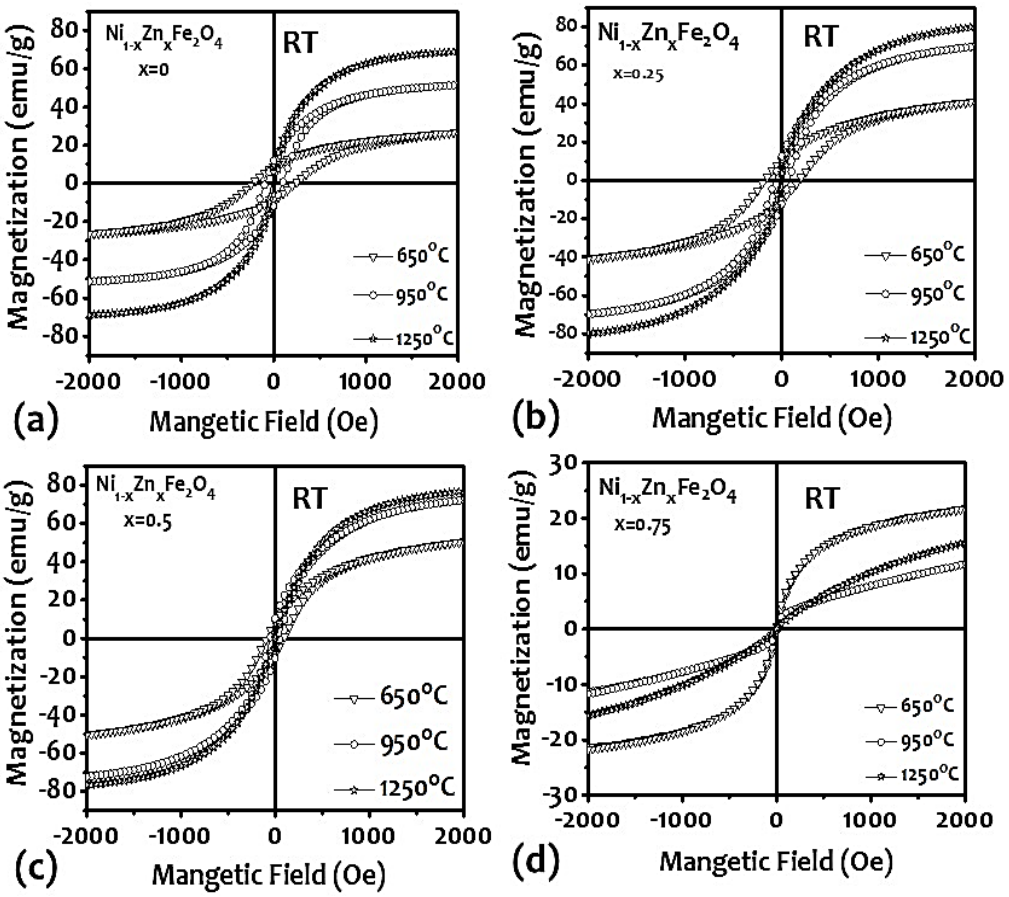

Figure 4.8 : Room-temperature M-H Hysteresis curves of $Ni_{1-x}Zn_xFe_2O_4$ ferrite powders at (a) x=0 (b) x=0.25 (c) x=0.50 (d) x=0.75

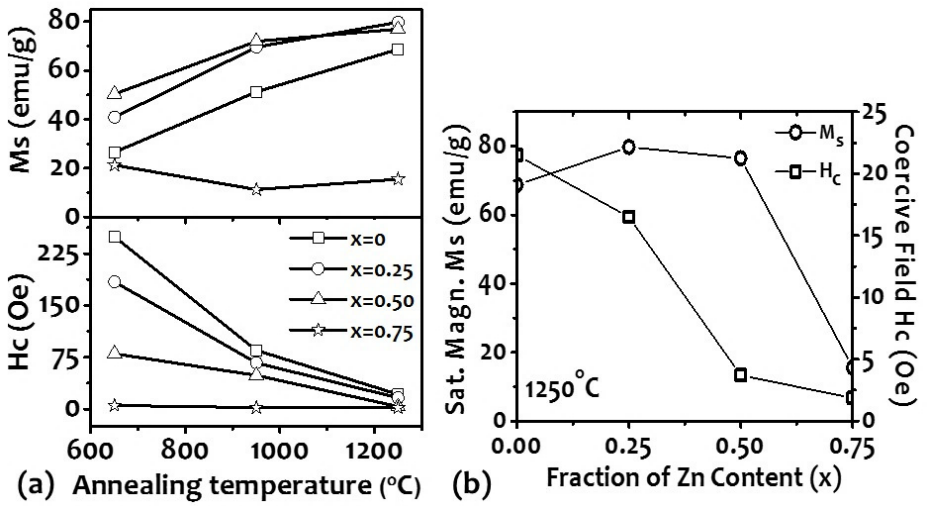

Figure 4.9 : Variation of saturation magnetization (M_s) & coercive field (H_c) with annealing temperature (b) Variation of M_s & H_c with fraction of Zn^{2+} ion content

4.3.6 Microwave Studies

4.3.6.1 Estimation of EM parameters of Ferrite Powders

The frequency dispersion of complex permittivity ($\varepsilon_r' = \varepsilon_r' - j\varepsilon_r''$) and permeability ($\mu_r = \mu_r' - j\mu_r''$) values are determined for all $Ni_{1-x}Zn_xFe_2O_4$ ferrite powders (x=0, 0.25, 0.50 and 0.75), annealed at different temperatures. All these $Ni_{1-x}Zn_xFe_2O_4$ samples, annealed at 1250°C, show similar values of $\varepsilon_r' \sim 6.3 \pm 0.1$ over the measured frequency range 2-12.4 GHz. The imaginary permittivity values exhibit a non-dispersive behavior with a constant value nearly ~0.005 for all the $Ni_{1-x}Zn_xFe_2O_4$ samples over the entire investigated frequency range. These measurements suggest that $Ni_{1-x}Zn_xFe_2O_4$ samples do not show any dielectric loss $\tan\delta_e$ ($= \varepsilon_r''/\varepsilon_r'$) over the frequency range 2-12.4 GHz due to negligible imaginary permittivity. The frequency dispersion characteristics of the complex permeability values are shown in Figures 4.10(a)-(d) for different ferrite compositions (x=0, 0.25, 0.50 and 0.75) annealed at 650°C, 950°C and 1250°C. The real permeability (μ_r') values are decreasing from ~2.5 to ~1 in the frequency range 2-12.4 GHz for ferrite compositions (x=0, 0.25, 0.50 and 0.75) annealed at different temperatures. However, the ferrite samples with the highest Zn^{2+} ions concentration (x = 0.75) shows nearly constant values over the entire frequency range of 2-12.4 GHz. Similarly, imaginary permeability (μ_r'') shows dispersion behavior for all these compositions except for the highest Zn^{2+} ions concentration (x=0.75). The complex permeability values change in the range from ~ -3.12 to -0.11 over the frequency range 2-12.4 GHz, with an increase in annealing temperatures. Imaginary permeability μ_r'' values exhibit increase in the lower frequency range (2-8 GHz) and the effect is more prominent for $Ni_{0.5}Zn_{0.5}Fe_2O_4$ sample. The imaginary permeability values vary from -1.90 to -0.11, -2.25 to -0.22 and -3.12 to -0.16 over 2-12.4 GHz for ferrite powder of composition x=0, x= 0.25 and x=0.5, respectively annealed at 1250°C. Further, the μ_r'' values are negligible ~0.02 for $Ni_{0.25}Zn_{0.75}Fe_2O_4$ samples, as shown in Figure 4.10(d). The variation is independent with the annealing temperature for this sample. These measurements suggest that annealing temperature as well as Zn^{2+} ion concentration in $Ni_{1-x}Zn_xFe_2O_4$ affect drastically the dispersive behavior of μ_r'' over the frequency range 2-12.4 GHz.

The imaginary permeability, which is responsible for MW energy loss, depends on saturation magnetization (M_s) and coercive field (H_c) as given in Eq. (4.1) [Zhang *et al.*, 2013]

$$\mu'' = \frac{M_S^2}{4\mu_0 K_1 \alpha} \quad \alpha \quad \frac{M_S^2}{H_c} \tag{4.1}$$

Where M_s is saturation magnetization, K_1 is anisotropic constant, α is Gilbert constant, H_c is coercive field and μ_0 is intrinsic permeability. These $Ni_{1-x}Zn_xFe_2O_4$ samples show an increase in saturation magnetization and decrease in coercive field values for compositions x=0, x=0.25, and x=0.5 with the annealing temperature. Therefore, μ_r'' values are increasing with the increase in annealing temperature from 650°C to 1250°C. Further, decrease in H_c values has also been observed with increase in Zn ion concentration for these ferrite compositions. As a result, μ'' values are found to increase from -1.90 to -3.2 at 2 GHz, with increasing Zn concentration from x=0 to x=0.5.

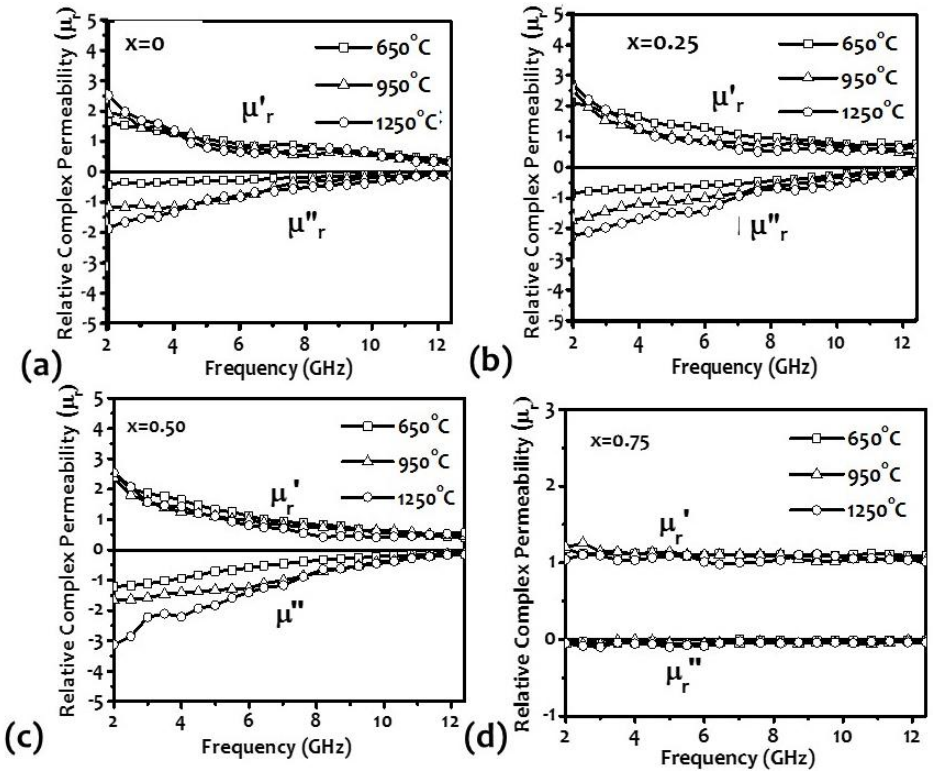

Figure 4.10 : Frequency dependence of the relative complex permeability for annealed $Ni_{1-x}Zn_xFe_2O_4$ powder (a) x=0 (b) x=0.25 (c) x=0.50 (d) x=0.75

4.3.6.2 Estimation of Loss Tangent Values for Ferrite Powders

The magnetic loss tangent ($\tan\delta_m$), which is the ratio of imaginary (μ_r'') and real part (μ_r') of permeability values, quantifies the loss behavior within the materials. The loss tangent values are plotted in Figures 4.11(a)-(d) for $Ni_{1-x}Zn_xFe_2O_4$ (x=0, 0.25, 0.50 and 0.75) ferrite powders annealed at different temperatures viz. 650°C, 950°C and 1250°C. From the Figures 4.11(a)-(c), we observe an increase in loss tangent values with both, increase in Zn concentration (x) from 0 to 0.5 and annealing temperature from 650°C to 1250°C for these ferrite samples. In case of samples annealed at 1250°C, the ferrite powder (x=0) shows loss tangent ($\tan\delta_m$) > 0.8 over 2-8 GHz with a maximum value ~ 1.27 at 6 GHz. The ferrite composition (x=0.25) shows enhanced loss tangent values > 0.8 over 2-10 GHz with a maximum value ~ -1.65 at 6 GHz. Further, ferrite composition (x=0.5) shows still higher values of loss tangent ($\tan\delta_m$) > -1.2 over 2 - 10 GHz with a maximum value ~ -1.75 at 6 GHz. It is observed that the ferrite composition with higher Zn^{2+} ion concentration (x=0.75) shows negligible loss characteristics over the entire frequency range. These observations are consistent with the observed behavior of saturation magnetization and coercive field values as described in the previous section 4.3.5. Further, it is interesting to note that the maximum loss tangent values for all compositions (x= 0, 0.25, 0.50 and 0.75) are found at 6 GHz. Figure 4.11(e) shows variation of maximum loss tangent $(\tan\delta_m)_{max}$ with Zn^{2+} ion concentration at resonating frequency of 6 GHz. We found that the $(\tan\delta_m)_{max}$ value increases with Zn^{2+} ion concentration up to x=0.50 and beyond that (at x=0.75) reduces sharply with negligible values found ~0.05.

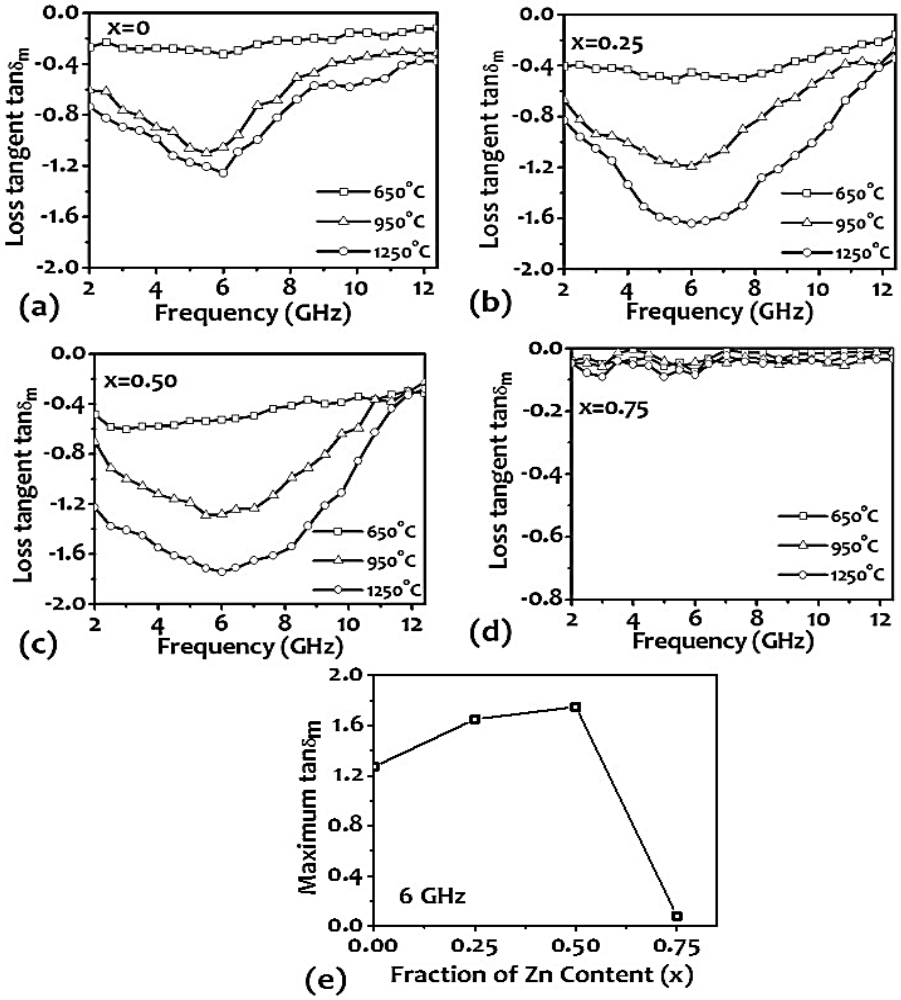

Figure 4.11 : Frequency dependence of the loss tangent ($\tan\delta_m$) for annealed $Ni_{1-x}Zn_xFe_2O_4$ powder (a) x=0 (b) x=0.25 (c) x=0.50 (d) x=0.75 (e) Variation of maximum loss tangent with Zn concentration at resonating frequency of 6 GHz.

The $Ni_{0.5}Zn_{0.5}Fe_2O_4$ ferrite powder annealed at 1250°C shows maximum loss tangent values among all other compositions, as explained in Figure 4.11(e). Considering the optimal magnetic parameters, this ($Ni_{0.5}Zn_{0.5}Fe_2O_4$) sample has been used for preparation of the rubber composites to investigate the microwave absorption properties over the frequency range 2-12.4 GHz.

4.3.6.3 Estimation of EM parameters and MW Loss Characteristics of Ferrite Loaded Rubber Composite

The different ferrite-NBR composite samples used for the present study were studied for their electromagnetic parameters viz. permittivity and permeability over 2-12.4 GHz frequency range. The measurements are summarized in Figures 4.12(a)-(c). 50wt% loaded ferrite-NBR sample, FMAR50, shows real component of permittivity value (ε_r') ~ 2.8±0.1 over the investigated frequency range. With the increase in ferrite filler loading, ε_r' value increases to ~ 4.2±0.2 at 60 wt% loading in sample FMAR60, ~ 4.7±0.1 at 70wt% in sample FMAR70 and ~5.9 at 80wt% loading in sample FMAR80 as summarized in Figure 4.12(a). The values of the imaginary component of the permittivity are found negligible between ~ 0.0015 and 0.002 over the entire frequency range of 2 - 12.4 GHz for all the ferrite loaded rubber composites, indicating the absence of dielectric loss behavior in rubber composites. Real component of the permeability values (μ_r') in rubber composite samples has shown decrease with increase in frequency, as shown in Figure 4.12(b). The μ_r' values for FMAR50, FMAR60, FMAR70, and FMAR80 lie in the range of 1.14 to 0.90, 1.25 to 0.80, 1.26 to 0.83 and 1.37 to 0.70 respectively. The values of the imaginary component of permeability (μ_r'') for FMAR50 sample found to be in the range of ~ -0.33 to -0.03 with a

reducing trend towards the lower frequency range. Further, enhancement in μ_r'' values for these composite samples was observed with increase in loading fraction of the ferrite powder samples. In FMAR60 sample, the μ_r'' shows more dispersion characteristics, with values in the range of ~ -0.65 to -0.10 over the entire frequency range. The μ_r'' values found to increase further in the range ~ -0.82 to -0.17 and ~ -1.03 to -0.20 for FMAR70 and FMAR80 samples respectively as shown in Figure 4.12(c).

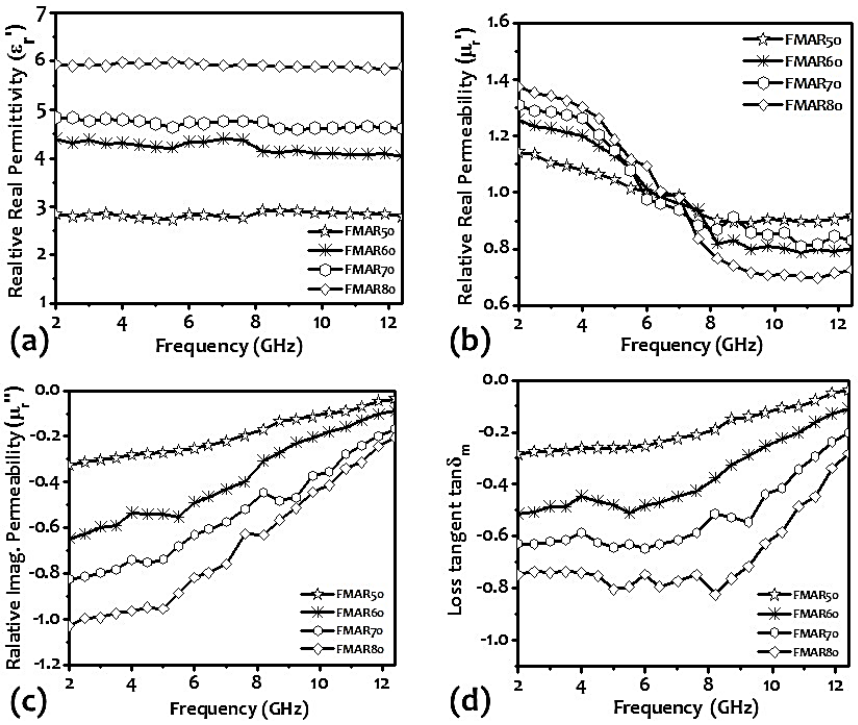

Figure 4.12: (a) Real permittivity plots for ferrite loaded rubber composites FMAR50-80 with MW frequencies (b) Real permeability behavior of ferrite loaded rubber composites (c) Imaginary permeability plots of ferrite loaded rubber composites (d) Loss tangent profiles for ferrite loaded rubber composites

Magnetic loss tangent ($\tan\delta_m$) plots are shown in Figure 4.12(d), for ferrite loaded rubber composites, FMAR50-FMAR80, in 2-12.4 GHz frequency range. The $\tan\delta_m$ values vary from ~-0.28 to -0.03 over 2-12.4 GHz with decreasing trend towards higher frequency range for FMAR50 composite sample. These values are enhanced in the range ~ -0.50 to -0.11, ~ -0.63 to -0.20 and ~ -0.80 to -0.30 in 2-12.4 GHz for FMAR60, FMAR70 and FMAR80 samples, respectively. The enhancement in loss tangent values for these composite samples has been attributed to the increase in the loading fraction of $Ni_{0.5}Zn_{0.5}Fe_2O_4$ ferrite in NBR by 1.50, 2.33 and 4.00 times in comparison to sample FMAR50 (Table-4.3).

4.3.6.4 Computation of Reflection Loss Characteristics

Based on above measured EM parameters, the MW reflection losses (R.L.) were computed for $Ni_{0.5}Zn_{0.5}Fe_2O_4$ ferrite loaded composite materials (FMAR50-FMAR80) by using the following Eq. (4.2) [Michielssen *et al.*, 1993].

$$R.L. = 20log_{10}\left|\frac{\sqrt{\frac{\mu_r^*}{\varepsilon_r^*}}tanh\left(\frac{j2\pi d}{\lambda_0}\sqrt{\mu_r^*\varepsilon_r^*}\right)-1}{\sqrt{\frac{\mu_r^*}{\varepsilon_r^*}}tanh\left(\frac{j2\pi d}{\lambda_0}\sqrt{\mu_r^*\varepsilon_r^*}\right)+1}\right| \quad (4.2)$$

Where, λ is the wavelength, $\mu_r^* = \mu_r' - j\mu_r''$ is the complex relative permeability, $\varepsilon_r^* = \varepsilon_r' - j\varepsilon_r''$is the complex relative permittivity and d is the absorber thickness. Further, the impedance of absorber's top layer should be comparable to the free space impedance Z_0 (377Ω) to enter MW inside the absorber for its effective attenuation as explained earlier in chapter 2. Considering the close approximation of matched wave impedance criterion, the reflection loss of the absorber has

been matched for absorber thickness (d_m) at $\lambda_m/4$, to satisfy the destructive interference between reflection surface and metal back reflecting surface, with the following dependence given in Eq. (4.3) and (4.4) [Petrov and Gagulin, 2001; Kim *et al.*, 1991].

$$\frac{4d}{\lambda} = \frac{\left(\sqrt{\mu_r'\varepsilon_r'}\right)}{(1+tan^2\,\delta_m)} \tag{4.3}$$

$$d_m = \frac{c}{4f\sqrt{|\mu_r^*||\varepsilon_r^*|}} \tag{4.4}$$

The calculated reflection loss values for different ferrite loaded samples are shown in Figure 4.14. The maximum possible reflection loss value $(R.L.)_{max}$ was ~ -4dB at 5 mm absorber thickness for FMAR50 sample. Further, composite samples with higher ferrite loading, FMAR60, the $(R.L.)_{max}$ value increased to ~ -10 dB for ~5 mm thickness, showing resonance at 7 GHz. Similarly, with further increase of ferrite loading (FMAR70), the $(R.L.)_{max}$ value increased to ~ -15 dB at 10 GHz, ~20 dB at 8.3 GHz and ~24 dB at 7 GHz for ~3.5 mm, 4.0 mm and 4.6 mm absorber thicknesses respectively. It is interesting to note that the absorption peak is shifting towards the lower frequency with increasing the absorber thickness for this composition.

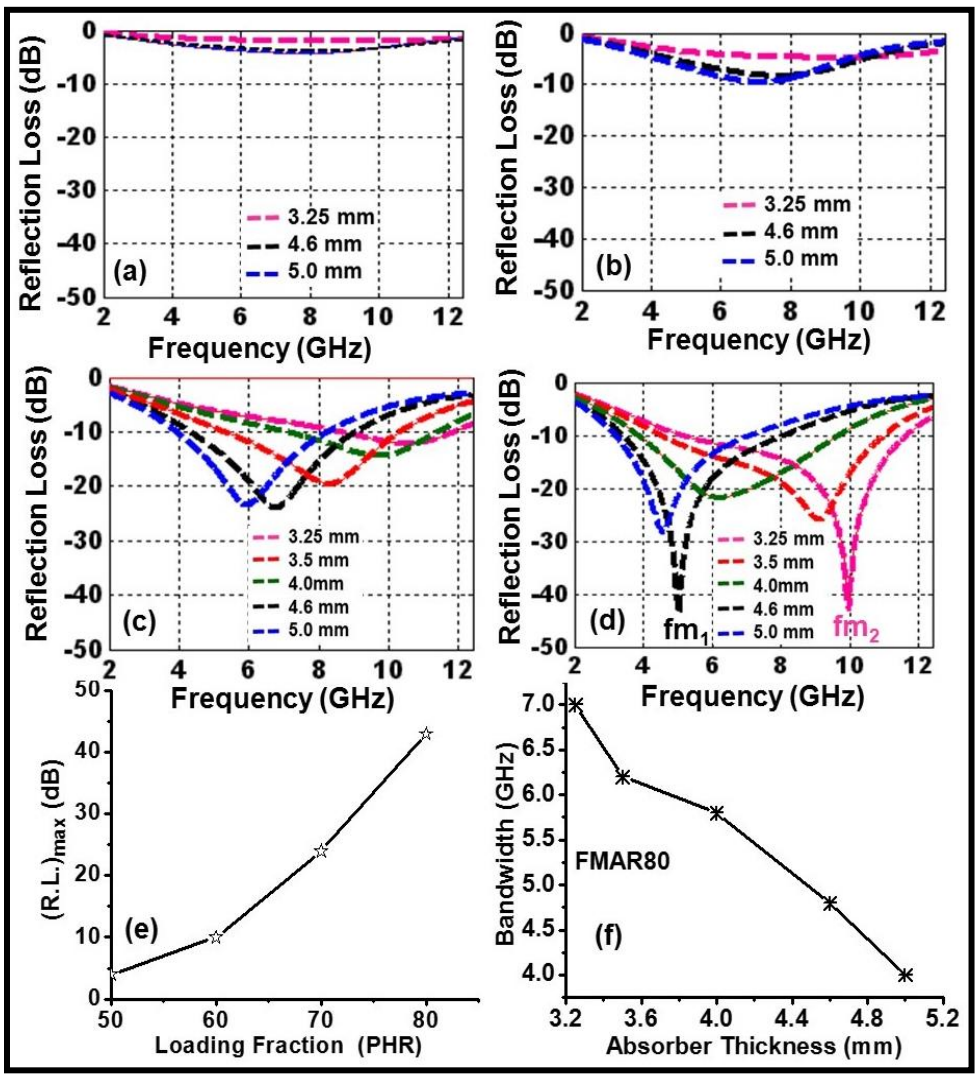

Figure 4.13 : Optimal Reflection Loss (R.L.) over frequency range 2-12.4 GHz and matching thicknesses of ferrite loaded rubber composites (a) FMAR50 (b) FMAR60 (c) FMAR70 (d) FMAR80 (e) Variation of maximum reflection loss with ferrite powder loading fraction in composite (f) Optimal R.L. bandwidth profile with composite absorber thickness

The observed shifting in reflection loss, towards lower frequency for FMAR70 composite can be explained using equations (4.3) and (4.4). These equations suggest that absorber thickness will effectively reduce with increasing ε_r' and $\tan\delta_m$. This is in agreement with the observed loss characteristics for FMAR70, as compared to FMAR50 and FMAR60 composite samples. The insignificant values of reflection loss observed for FMAR50 and FMAR60 are mainly due to very low magnetic loss tangent values, shown by these composites. Interestingly, at higher loading of ferrite for FMAR80 composite sample, twin match frequencies (f_{m1}/f_{m2}) are observed at two matched thicknesses (t_{m1} and t_{m2}) [Figure 4.14 (d)]. At absorber thickness t_{m1}=4.6 mm, the first matched $(R.L.)_{max}$ value observed is ~ -43 dB at matching frequency f_{m1} ~ 5 GHz. With the decrease in absorber thickness, R.L profile has shifted towards higher frequency side with lower $(R.L.)_{max}$ values ~ -26 dB and ~ -22 dB for absorber thicknesses ~ 4mm and 3.5 mm, respectively. Further reduction in absorber thickness at t_{m2} = 3.25 mm, the second matched $(R.L.)_{max}$ value has been observed ~ -43 dB at twin matching frequency f_{m2} ~10 GHz.

Naito *et al*. reported the existence of two matching frequencies in ferrite based EM wave absorbers [Naito and Suetake, 1971]. Further, Shin *et al.* have also observed two matching frequencies f_{m1} and f_{m2} in Ni substituted Y-type barium hexaferrite (Ni_2Y) sintered samples and single matching frequency in Ni_2Y-rubber composites [Shin and Oh, 1993]. The two possible MW absorption loss mechanisms are generally attributed in the ferrite materials and their composites: (i) relaxation mechanism due to the domain wall motion and (ii) spin rotational resonance due to the spin magnetic moment response. The domain wall resonance mechanism is responsible for magnetic losses at lower MW frequency range (< 1 GHz) as relaxation of domain motion cannot follow the higher MW frequency response beyond 1 GHz. The relaxation of spin resonance follows the higher MW frequencies and therefore, ferromagnetic resonance (FMR) is responsible in ferrites for a particular frequency range, resulting in the absorption of incident MW radiation. The maximum loss tangent value observed is at 6 GHz for 1250°C annealed $Ni_{0.5}Zn_{0.5}Fe_2O_4$ ferrite powder. It is close to the first matching frequency (f_{m1}) observed at ~5 GHz for 4.6 mm thick FMAR80 sample, Figure 4.13(d). This is attributed to the spin resonance relaxation mechanism in the ferrite loaded rubber composites. The second matching frequency (f_{m2}) has been observed at ~10 GHz for 3.25 mm FMAR80 absorber thickness. The f_{m2} is independent of resonance frequency and onset of this resonance is due to the matched thickness of absorber ($\lambda_m/4$~ 3.25 mm), as given by equation (4.4). The R.L. profile associated to f_{m1} at absorber thickness ~ 3.25 mm may extend towards higher frequency side (a blue shift) with a decrease in thickness. In contrast, the R.L. profile associated with f_{m2} may shift towards the lower frequency side (a red shift) with an increase in thickness up to 4 mm. that the observed R.L. profile can be understood by considering both the components of matching frequencies as ($x.f_{m1} + y.f_{m2}$) at these thicknesses, where x and y are the fractional contribution from individual matching frequencies. At the intermediate absorber thickness of 3.5 mm and 4.0 mm the matching frequency (f_M) behavior follows the trend as given in Eq. (4.5) and (4.6), respectively

$$d= 3.5 \text{ mm}; f_M = x.fm_1 + y.fm_2, \text{ while } x < y \quad (4.5)$$

$$d= 4.0 \text{ mm}; f_M = x.fm_1 + y.fm_2, \text{ while } x > y \quad (4.6)$$

The resonance frequencies for d = 3.5 mm and 4.0 mm thick FMAR80 samples are ~10 and ~5 GHz respectively, as shown in Figure 4.13(d). The Eq. (4.5) and (4.6) have been used to estimate the fractional x and y contributions for both the matching frequencies f_{m1} and f_{m2} respectively. The calculated fractional contributions for d = 3.5 mm thick FMAR80 sample are x = 0.2 and y = 0.8 corresponding to f_{m1} (5 GHz) and f_{m2} (10 GHz) respectively and for d = 4.0 mm thick FMAR80 sample are x = 0.8 and y = 0.2 corresponding to f_{m1} (5 GHz) and f_{m2} (10 GHz) respectively, substantiating the proposed contribution of two matching frequencies.

In addition, we observed that the maximum reflection loss $(R.L.)_{max}$ values for rubber composites increase with increasing the loading fraction of ferrite powder as shown in Figure 4.13(e). Interestingly, for FMAR80, the desired frequency bandwidth (where R.L. ≥ 10 dB or at

least 90% attenuation of MW signal) decreases with absorber thickness as shown in Figure 4.13(f). The MW absorber at 3.25 mm thickness (corresponding to f_{m1}) has the widest bandwidth of 7 GHz with $(R.L.)_{max}$ values of ~ -43dB. The frequency bandwidth window reduces to ~ 4.2 GHz with the same value of $(R.L.)_{max}$ at 4.6 mm absorber thickness. In the intermediate thicknesses, the bandwidth lies in between this range. Therefore, the MW frequency operational range can be tailored by varying the thickness as a controlling parameter for the FMAR80 composite sample with the optimal R.L. values. This makes FMAR80 a compatible material for the desired MW absorption application over different frequency bands.

4.4 CONCLUDING REMARKS

In conclusion, phase pure $Ni_{1-x}Zn_xFe_2O_4$ (x=0, 0.25, 0.5, 0.75) ferrite powders have been synthesized by using simple and cost-effective gel to carbonate precipitation method, followed by sequential annealing at 650°C, 950°C and 1250°C temperatures. The modification of structural and magnetic properties of $Ni_{1-x}Zn_xFe_2O_4$ powders have been observed with the increase in annealing temperature and 1250°C annealed $Ni_{0.5}Zn_{0.5}Fe_2O_4$ have shown the highest loss tangent > -1.20 over the entire frequency range 2-10 GHz of interest. These studies suggest that $Ni_{0.5}Zn_{0.5}Fe_2O_4$ material may be a good choice as filler in NBR matrix for microwave absorption applications. The R.L. values of 80wt% loaded $Ni_{0.5}Zn_{0.5}Fe_2O_4$/NBR composites show twin matching frequencies for two MW resonant absorption peaks in 2-12.4 GHz frequency range. The first matching frequency (f_{m1}) observed at ~ 5 GHz corresponds to $(R.L.)_{max}$ values ~ 43 dB for thickness ~4.6 mm and is induced by magnetic spin relaxation process, whereas the second matching frequency (f_{m2}) at ~10 GHz with same R.L. values ~ 43 dB at thickness ~3.25 mm, is attributed to the matched quarter wave thickness of absorber.

...